

## Factors Affecting ENSO's Period

DOUGLAS G. MACMYNOWSKI

*Control and Dynamical Systems, California Institute of Technology, Pasadena, California*

ELI TZIPERMAN

*Department of Earth and Planetary Sciences, School of Engineering and Applied Sciences, Harvard University, Cambridge, Massachusetts*

(Manuscript received 21 May 2007, in final form 4 September 2007)

### ABSTRACT

Accurately capturing the observed mean period of ENSO in general circulation models (GCMs) is often challenging, and it is therefore useful to understand which parameters and processes affect this period. A computationally efficient simulation-based approach is used to extract both the dominant eigenvalues and corresponding eigenvectors of the linearized model from the Zebiak–Cane intermediate-complexity model of ENSO without having to directly construct the linearization. The sensitivity of the period to a variety of parameters is examined, including atmosphere–ocean coupling, atmospheric heating parameterization, thermocline depth zonal profile, western boundary reflection coefficient, atmospheric and ocean wave speeds or Rossby radii of deformation, ocean decay time, and the strength of the annual cycle. In addition to the sensitivity information, the spatial structures of the main fields (SST, thermocline thickness, and more) that are involved in period changes are obtained to aid in the physical interpretation of the sensitivities.

There are three main time lags that together compose one-half of a model ENSO period: the Rossby-plus-Kelvin wave propagation time for a wind-caused central Pacific disturbance to propagate to the western ocean and back, SST dynamics that determine the lag between eastern ocean thermocline anomalies and eastern ocean SST anomalies, and the “accumulation” lag of integrating a sufficient delayed wave signal arriving from the western ocean to cancel the eastern ocean anomalies. For any of the parameter changes considered, the eigenvector changes show that the largest contributor to the period change is from changes to the last of these three mechanisms. Physical mechanisms that affect this accumulation delay are discussed, and the case is made that any significant change to ENSO's period is in turn likely to involve changes to this delay.

---

### 1. Introduction

ENSO's period varies between 2 and 7 yr, with the average being quite robust around 4 yr. Accurately capturing the observed periodicity in GCMs nonetheless still seems elusive (e.g., Timmermann et al. 1999; Doherty and Hulme 2002; AchutaRao and Sperber 2002, 2006; Collins et al. 2005) and often requires tuning parameters somewhat arbitrarily. It is thus valuable to describe the sensitivity of the period to as many relevant parameters as possible to enhance our understanding of which parameters and physical processes

are most important and to provide guidance on improving GCM ENSO simulations.

The observed irregular periodicity has been explained either as the result of self-sustained, possibly chaotic behavior (Jin et al. 1994; Tziperman et al. 1994, 1995), such as the output of a damped stable system driven by weather “noise” external to the ENSO dynamics excited through nonnormal growth (Kleeman and Moore 1997; Penland and Sardeshmukh 1995; Burgers 1999; Philander and Fedorov 2003; Wang et al. 1999; Thompson and Battisti 2000), or as a combination of the two (Kirtman and Schopf 1998). In either case, ENSO models have a dominant complex (oscillatory) eigenvalue pair that is either stable (damped) or unstable (self-sustained behavior) and whose period is related to the observed ENSO periodicity. Understanding the behavior of these dominant eigenvalues of the

---

*Corresponding author address:* Douglas G. MacMynowski, Control and Dynamical Systems, California Institute of Technology, 1200 E. California Blvd., M/C 107-81, Pasadena, CA 91125.  
E-mail: macmardg@cds.caltech.edu

linearized system as a function of model parameters is therefore useful in understanding the dynamics. If the system is stable and forced by external noise, variations in the eigenvalue can directly describe the variation expected in the time series. In the self-sustained or chaotic cases, the behavior of the eigenvalues is still useful in describing the output, although nonlinear effects will certainly be relevant in this case and can also affect the period (Münnich et al. 1991; Jin 1997a,b; Eccles and Tziperman 2004).

The variation in the dominant eigenvalues of a linearized ENSO model as a function of one or more parameters is a well-established approach that has proven useful in understanding ENSO dynamics (Jin and Neelin 1993a; Neelin et al. 1994; Jin et al. 1996; Thompson and Battisti 2000, 2001; Dijkstra 2000; An et al. 2004; Cane et al. 1990). These studies either considered relatively simple ENSO models, in which the combined effects of multiple physical processes are lumped together into a few key parameters, or considered only a few parameters in more complex models.

Ocean–atmosphere coupling is a key parameter explored in bifurcation analysis of ENSO models as summarized, for example, by Dijkstra (2000). Jin and Neelin (1993a) considered a “stripped-down” version of the Zebiak and Cane (1987) model (hereafter ZC model) that retains the essential behavior but allows some analytical results to be generated. Eigenvalue behavior is plotted (e.g., Neelin et al. 1994) as a function of the wind stress coupling coefficient, the relative adjustment time between oceanic wave dynamics and SST adjustment, and a surface-layer parameter. Thompson and Battisti (2000, 2001) used a linearized version of an intermediate complexity model (Battisti 1988) similar to the ZC model and considered the wind stress coupling factor, the western boundary reflection coefficient (WBRC), and the ocean damping time constant. Eigenvalue variation was also used by An et al. (2004) to understand the influence of changes in the background climate state on ENSO dynamics during the Last Glacial Maximum (LGM). In addition, both Thompson and Battisti (2000) and Van der Vaart et al. (2000) plotted the eigenvector for standard parameter choices in an intermediate complexity model.

In addition to these eigenvalue variation studies, several studies describe impacts of variations of specific parameters on ENSO. Zebiak and Cane (1987) explored some parametric sensitivities through time simulations. Van der Vaart et al. (2000) illustrated that the recharge oscillator of Jin (1997a) is a good metaphor for the dominant mode in a ZC-type model and that the spatial shape of this mode is strongly influenced by the background climatology. One of the strongest influ-

ences on the period was found to be the ratio of atmosphere and ocean Rossby radii of deformation. This ratio affects the meridional structure of ocean Rossby waves excited by the wind forcing, with the resulting impact on ENSO’s period described in detail by Kirtman (1997). The importance of eastern Pacific thermocline depth has been noted in numerous contexts (e.g., Timmermann et al. 1999, 2005; Fedorov and Philander 2001; Philander and Fedorov 2003; Münnich et al. 1991; Galanti et al. 2002). Philander and Fedorov also noted the importance of the temperature gradient across the thermocline. The importance of wave reflection coefficients (Kang and An 1998), vertical mixing (Syu and Neelin 2000), and the background mean state (Codron et al. 2001) have been studied.

The purpose of this paper is to obtain additional insight into the factors determining and affecting ENSO’s period. Our approach, similar to that of the above studies, is to explore both the eigenvalue and the eigenvector behaviors as a function of many different parameters in the ZC model. We introduce two novel elements into our analysis. First, we vary a combination of more than one parameter to create a change to the period of ENSO without changing the amount of damping of the ENSO mode. This allows us to try to understand what affects ENSO’s period specifically. Second, we explore the dependence of the period in the ZC intermediate-complexity model on many more parameters than have previously been described by utilizing a novel technique of efficiently extracting the desired eigenvalue information from carefully constructed simulations without having to explicitly construct the linearization of the model. This technique can, in principle, be extended to more complex models. This approach of using a set of short simulations to extract relevant low-dimensional information from high-dimensional numerical models has been extensively explored in the control engineering literature by Kevrekidis et al. (2003, 2004).

Using this technique, we find that changes to the period of ENSO can result from changes to one of three possible delays that affect it: the wave propagation delay (Suarez and Schopf 1988; Battisti 1988), the accumulation delay (Cane et al. 1990; Kirtman 1997), or the SST dynamics delay in the eastern Pacific (Jin and Neelin 1993a,b; Neelin and Jin 1993). Accumulation delay is a term introduced by Cane et al. (1990) for the delay in accumulating enough negative feedback from the delayed Rossby waves to eliminate the positive anomaly that has developed in the eastern Pacific because of the Kelvin waves. We find that changes to this accumulation delay seem to be the main reason for the period changes we identify in our experiments.

The next section describes the relevant background to the approach used here, including a brief summary of the relevant aspects of the ZC model and the algorithms used here for extracting both eigenvalues and eigenvectors. The sensitivities to a change in a single parameter at a time and then to a simultaneous change in two parameters are described in sections 3a, b, respectively, and we conclude in section 4.

## 2. Methodology

### a. Zebiak–Cane model parameters

We use the intermediate-complexity coupled atmosphere–ocean ZC model of the tropical Pacific, which computes perturbations about a specified monthly climatology. The model parameters that we vary to study their effect on ENSO’s period are as follows:

- the drag coefficient  $R^*$  that determines the wind stress given the atmospheric wind speed, and hence determines the strength of the ocean response to atmospheric winds;
- several parameters in the atmospheric heating parameterization, including
  - $\alpha$ , which scales the atmospheric heating because of SST-dependent evaporation, and
  - $\beta$ , which scales the atmospheric heating because of large-scale atmospheric wind (and therefore moisture) convergence;
- the specified mean thermocline depth zonal profile  $\bar{h}$ ; only the eastern thermocline depth is changed here while the (deeper) western thermocline depth is kept fixed (the mean thermocline depth is also an effective ocean–atmosphere coupling coefficient); a deeper mean thermocline means that changes to the thermocline depth due to wind anomalies have a weaker effect on the SST, and therefore on the atmosphere;
- the ocean western boundary reflection coefficient (amplitude of eastward-traveling Kelvin wave in response to an incident westward-traveling Rossby wave);
- the atmosphere Rossby radius of deformation or, equivalently, the atmosphere wave propagation speed  $c_a$ ;
- the ocean-layer depth used in computing ocean wave propagation speeds [ $H$  in (A.6) of Zebiak and Cane 1987] or the equivalent depth  $h_{\text{equiv}}$ ;
- the ocean momentum damping time  $T_{\text{decay}}$ ; and
- the strength of the annual cycle, with two different cases noted in particular:
  - a coefficient that determines the amplitude of the seasonal cycle relative to the annual mean state and

TABLE 1. Standard values of parameters in ZC model.

Parameter	Value	Parameter	Value
$R^*$	1.0	$T_{\text{decay}}$	30 months
$\alpha$	1.6	WBRC	1.0
$\beta$	0.75	$c_a$	60 m s <sup>−1</sup>
$\bar{h}$	50 m	$h_{\text{equiv}}$	0.86 m

- a coefficient that determines the amplitude of the seasonal cycle relative to the state of permanent July conditions (chosen because it is a highly unstable month).

With the standard values for the parameters used in Zebiak and Cane (1987), given for reference in Table 1, the background state is linearly unstable and the ENSO variability is self-sustained and chaotic (Tziperman et al. 1995). We examine the sensitivity of the period under both this standard regime and a linearly damped oscillatory regime.

### b. Eigenvalue analysis

Let a state vector  $\mathbf{x}_k$  at time  $t_k$  include all of the prognostic variables required to determine the future evolution of the ZC model. This includes the SST at each grid point and the oceanic Kelvin and Rossby wave amplitudes. In addition, although the atmosphere is assumed to reach equilibrium rapidly and its time derivatives are neglected in the model equations, the iterative numerical solution starts from the previous time step solution and does not necessarily converge at each time step. Thus the atmospheric fields depend on their value during the previous time step and are therefore part of the state vector of the ZC numerical model. With the  $78 \times 116$  ocean dynamics grid points and  $30 \times 34$  SST and atmospheric dynamics grid points, this leads to a total of  $N_{\text{state}} = 32\,903$  state variables.

The nonlinear time stepping numerical model can be written as

$$\mathbf{x}_{k+1} = \mathbf{f}(\mathbf{x}_k, m), \quad (1)$$

where  $m = 1, \dots, 12$  determines the monthly background fields and therefore influences the dynamics. Because this model computes perturbations about the background state, the zero state  $\mathbf{x} = 0$  is a solution (fixed point or equilibrium point) of the model equations. The ZC model uses 3 time steps per month, which can be combined to give an iteration as above where  $k$  is a monthly time index.

The time-periodic system can be converted to a time-invariant system through Floquet analysis (Iooss and Joseph 1990), as has been done for ENSO models by Jin et al. (1996), Thompson and Battisti (2000), and

Samelson and Tziperman (2001). More simply put, we can write an annual model as

$$\mathbf{x}_{k+12} = \mathbf{g}_m(\mathbf{x}_k), \quad (2)$$

where  $\mathbf{g}_m$  is obtained by iterating (1) for 1 yr starting from month  $m$  and relates the state at the end of one month to the state 1 yr earlier. In this formulation, the rhs does not depend on time explicitly (model is autonomous).

The eigenvalues  $\lambda$  and corresponding eigenvectors  $\mathbf{v}$  of the linearized model are defined to be those of the appropriate Jacobian matrix of the nonlinear model equations,

$$\mathbf{J}_m \mathbf{v} \equiv \frac{\partial \mathbf{g}_m}{\partial \mathbf{x}} \mathbf{v} = \lambda \mathbf{v}. \quad (3)$$

Furthermore, the eigenvalues of this annual model propagator do not depend on the month  $m$ , although in general the eigenvectors do. Because this is a discrete-time system, the magnitude of the eigenvalue of  $\mathbf{J}_m$  determines the annual growth rate and stability ( $|\lambda| > 1$  being unstable;  $|\lambda| < 1$  being stable) and the phase of the complex eigenvalue determines the period.

The least stable mode (which is a pair of complex-conjugate eigenvalues) of the annual model is the most important for describing the dynamics of ENSO, although other modes may clearly be important because of the potential for nonnormal growth (Penland and Sardeshmukh 1995; Kleeman and Moore 1997; Thompson and Battisti 2000, 2001). For the standard parameters used in the original ZC model, we find by using the methodology outlined below that the least stable mode has a period of roughly 3.4 yr and an annual growth factor of 1.25; these are slightly different from the values in Thompson and Battisti (2000) because of different choices of parameters and details of the model formulation.

The sensitivity analysis in this paper is based on the linearized model, yet it is straightforward to show by numerical simulations that for the standard parameters in the ZC model, the sensitivity of the period and damping of the full model is the same as that deduced from the dominant eigenvalue of the linearized model. We also note that the nonlinear phase-locking to the seasonal cycle leads to potentially discontinuous period changes in response to continuous shifts in model parameters (Fig. 15 in Neelin et al. 2000).

### c. Eigenvalue/eigenvector calculation algorithm

The eigenvalue calculation algorithm used here is based on running relatively short numerical simulations and analyzing the output time series to extract the

eigenvalues without having to explicitly construct the linearization. The method can, in principle, be applied to much more complicated models, although it would need to be extended to include the calculation of the equilibrium state if that is nonzero. (Readers who are interested in the sensitivity of ENSO's period but not in the algorithm used here are invited to skip to section 3.)

The algorithm is quite straightforward for the ZC model because it is an anomaly model; that is, the equilibrium state is zero. The only code modification required is to introduce a scale factor on the entire state vector at each iteration. Thus, rather than integrating the original nonlinear system  $\mathbf{x}_{k+1} = \mathbf{f}(\mathbf{x}_k, m)$ , we integrate the modified system

$$\mathbf{x}_{k+1} = \gamma \mathbf{f}(\mathbf{x}_k, m). \quad (4)$$

Choosing an appropriate scale factor  $\gamma$  guarantees that the simulation is stable and thus that nonlinear effects can be minimized by selecting sufficiently small initial conditions. The eigenvalues of the scaled system are related to those of the original system by the scale factor

$$\lambda \left[ \frac{\partial(\gamma \mathbf{f})}{\partial \mathbf{x}} \right] = \gamma \lambda \left( \frac{\partial \mathbf{f}}{\partial \mathbf{x}} \right), \quad (5)$$

and the eigenvalues of the annual system in (3) scale with  $\gamma^{12}\lambda$ . The scaling is therefore equivalent to adding ( $\gamma < 1$ ) or removing ( $\gamma > 1$ ) numerical damping, and it can be used not just to stabilize the system but to choose the system stability so that the dominant eigenmode is lightly damped and decays slowly. This helps minimize the error in estimating the eigenvalues for a given amount of computation. If this technique is applied to a system in which the equilibrium state is nonzero, the scaling should be applied to the perturbation about the equilibrium.

We calculate the dominant eigenvalues from the unforced time series model response to an initial perturbation. The unforced response of a linear oscillatory system with a single mode will simply be a sinusoid decaying or growing with time. For a system with multiple modes, the response will eventually be dominated by the least stable mode. Any initial condition  $\mathbf{x}_0$  can be expressed as a linear combination of eigenvectors of the linearized Jacobian  $\mathbf{J}_m$  (3),  $\mathbf{x}_0 = \sum_1^N \alpha_j \mathbf{v}_j$ , where  $\mathbf{J}_m \mathbf{v}_j = \lambda_j \mathbf{v}_j$  and  $\lambda_j = |\lambda_j| e^{i\phi_j}$ . For a (oscillatory) complex-conjugate dominant eigenvalue pair,  $\lambda_2 = \lambda_1^*$  and  $\mathbf{v}_2 = \mathbf{v}_1^*$ , and for a sufficiently large time  $k$ , all modes decay except for the first, so that

$$\mathbf{x}_k = \mathbf{J}_m^k \mathbf{x}_0 \simeq |\lambda_1|^k (\alpha_1 e^{ki\phi_1} \mathbf{v}_1 + \alpha_1^* e^{-ki\phi_1} \mathbf{v}_1^*). \quad (6)$$

It is sufficient to estimate the eigenmodes of the system using the time series of a scalar (or in general, some

low  $M$ -dimensional) model output  $\mathbf{y}_k$ , which is a function of the full state vector rather than using the full state, provided that the dynamics of interest are observable in the chosen output. The estimation algorithm converges using the minimum length of a model output time series given an output variable  $\mathbf{y}_k$ , in which the ENSO mode is most observable. We use for  $\mathbf{y}_k$  the model-computed monthly Niño-3 index (scalar average SST over  $5^\circ\text{N}$ – $5^\circ\text{S}$ ,  $150^\circ$ – $90^\circ\text{W}$  of the equatorial eastern Pacific, so that  $M = 1$ ) because it clearly reflects the behavior of the ENSO mode and the spatial averaging reduces the contamination with high-spatial-frequency dynamics.

We use an autoregressive (AR) model (also used to fit the observed ENSO data by Burgers 1999) to fit the model output data and evaluate the eigenvalues of the AR model. The AR model assumes that the model output  $\mathbf{y}_k$  at time  $t_k$  can be described in terms of the output at a finite number  $N$  of previous outputs, which for the annual model takes the form of

$$\mathbf{y}_k = \sum_{n=1}^N a_n \mathbf{y}_{k-12n}, \quad (7)$$

with coefficients  $a_n$  that are the same regardless to which month the index  $k$  corresponds, because the eigenvalues of the annual evolution do not depend on the month. The eigenvalues of the discrete-time system (7) are the roots of the polynomial

$$p(\lambda) = 1 - a_1\lambda - a_2\lambda^2 - \dots - a_N\lambda^N. \quad (8)$$

The coefficients  $a_i$  (and therefore the eigenvalues) are estimated from the model output time series using a recursive formulation so that the convergence can be monitored to avoid unnecessary extra simulation. The algorithm details are provided in appendix A.

An example plot of a simulated time history and a comparison with AR fit (7) is shown in Fig. 1. The AR fit is clearly satisfactory, indicating that the extracted eigenvalues (and eigenvectors whose calculation is described below) may be expected to be reasonably accurate. Note that the irregularity in Fig. 1 is associated with the seasonal cycle, not with nonlinearities or additional dynamics.

The estimation algorithm proceeds as follows: given an initial guess for the estimated parameters  $a_i$ , choose the initial conditions and a scale factor  $\gamma$ , run a short simulation, update the parameter estimate, extend the simulation if needed, and iterate until converged.

Several issues affect the calculation accuracy and the simulation length required to achieve a specified tolerance. For any linearizable system, nonlinear effects in the response can be made sufficiently small by choosing a sufficiently small initial condition. However, in prac-

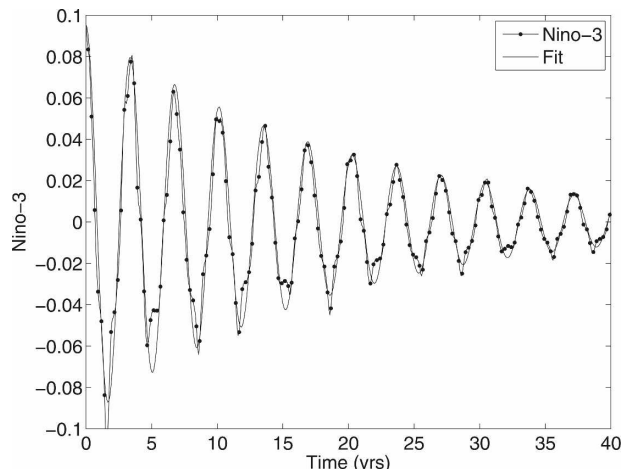


FIG. 1. Representative time history of model Niño-3 index (dotted every 3 months) and fourth-order fit (solid) used to calculate the eigenvalues and eigenvectors of the linearized model.

tice, the amplitudes are limited by small-amplitude numerical noise such as roundoff errors. Nonlinear effects are minimized by choosing small-amplitude initial conditions, choosing the scale factor so that the dominant eigenvalue is lightly damped, and rescaling the initial condition back into the desired range after each short period of simulation. Once the calculation has started, the desired scale factor can easily be estimated with sufficient accuracy based on the current estimate of the ENSO eigenvalue damping from (8) and the desired damping [we use  $\gamma$  values for each parameter regime such that  $\gamma^{12}|\lambda| = 0.95$ ; see (5)]. Choosing an initial condition as close as possible to the eigenvector of the desired mode, if known, minimizes the contribution in the response due to other modes; however, nonnormal growth can always occur unless the initial condition is exactly aligned with the eigenvector of the dominant eigenvalue. Better accuracy is therefore obtained by fitting a fourth-order AR model to calculate two modes simultaneously; that is, we use  $N = 4$  in (7) to obtain the results shown below.

As evident from (6), after sufficient time the response is dominated by the least-damped eigenvector. Given a time history of the full state output  $\mathbf{x}$  over an integer number of ENSO periods, the eigenvector corresponding to the largest eigenvalue  $\lambda$  can be estimated from the weighted average

$$\mathbf{v} = \frac{1}{m+1} \sum_{k=0}^m \lambda^{-k} \mathbf{x}_{k_0+k}. \quad (9)$$

Note that the second term in (6) involving the complex conjugate of  $\mathbf{v}$  yields zero when averaged over an integer number of ENSO periods.

The eigenvector is only unique up to a complex scalar factor  $re^{i\theta}$ . We choose the phase  $\theta$  so that the real part of the eigenvector corresponds to the state of the model at the time of maximum Niño-3 index, by choosing  $k_0$  in (9) to be at the time of a Niño-3 maximum. The eigenvector magnitude is normalized by  $r$ , which is set to the inverse spatial RMS of the SST component of the eigenvector. The eigenvector of the annual model depends on the month, and plots shown here are for the eigenvector averaged over 12 months, as obtained directly from the averaging in (9).

Each computed eigenvector includes all elements of the state vector, but we plot below only four main variables defined on the sea surface grid: the SST anomaly, the thermocline depth anomaly, the ocean zonal current anomaly, and the resulting atmospheric zonal wind anomaly. If desired, additional eigenvalues and eigenvectors could be calculated by first finding the dominant eigenvalue/eigenvector, and then subtracting the projection of this eigenvector from the initial condition.

There is one numerical detail that is especially relevant in our subsequent analysis. The iterative solution for the atmosphere in the original ZC code is occasionally reset to start from a zero field to avoid converging into spurious atmospheric states. The default strategy for doing so resets the atmosphere initial guess whenever the computed Niño-3 index is sufficiently small, resulting in a slightly different set of dynamics for the (small amplitude) linearized model. The impact of the atmosphere resetting algorithm on the linearization will be discussed in section 3.

### 3. Sensitivity of ENSO's period to model parameters

We consider first a fairly straightforward description of the sensitivity of the model to a perturbation in one parameter at a time (section 3a). Next, to isolate processes that affect ENSO's period, we perform experiments in which two parameters are varied simultaneously to create a change to the period only, with no change to the damping of the ENSO mode (section 3b). This last subsection explores some interesting insights regarding ENSO's period.

#### a. Single-parameter sensitivity experiments

The key parameters to which we explore the sensitivity of model dynamics are listed in section 2a. Eigenvalues, eigenvectors, and root loci (plots of eigenvalues as a function of model parameters) are computed in four different regimes in parameter space:

Regime A: Baseline parameters in Zebiak and Cane (1987), including the seasonal cycle, with the drag

coefficient (which may be viewed as an ocean-atmosphere coupling parameter) set to  $R^* = 1$ . The basic background state is linearly unstable in this case, and we set the scaling factor to  $\gamma = 0.9774$  (at each monthly time step) to stabilize the model (5) and give a scaled eigenvalue magnitude of 0.95.

Regime B: Reduced drag coefficient of  $R^* = 0.75$  so that the linearization is stable. (The stability boundary is roughly at  $R^* = 0.79$ , so this guarantees that the system is more than slightly stable.)

Regime C: Seasonal cycle turned off, with background fields replaced by the annual mean. The linearization is stable in this case even with  $R^* = 1$ .

Regime D: Seasonal cycle turned off, with background fields replaced by permanent July conditions, giving a highly unstable system ( $\gamma = 0.9458$  gives  $\gamma^{12}|\lambda| = 0.95$ ).

Computing the parametric dependence of ENSO's period at these four different regimes helps to assess the robustness of the parameter sensitivity results. In particular, we can find out if the results depend on whether the model is self-sustained/chaotic or damped (stable) and on whether the model is time periodic (nonautonomous, first two regimes above) or time invariant (last two regimes).

The eigenvalue period and growth rate are plotted as a function of parameter values around these four locations in parameter space in Fig. 2. The period is obtained from the phase of the complex eigenvalue, while the growth rate is the magnitude of the eigenvalue, with magnitude one giving the boundary between stable and unstable responses. Note that the scales are different for each regime. Each 5% variation in parameter value is marked on the curves, so the period sensitivity is high for those parameters whose curves are mostly horizontal and have large spacing of line markers. Figure 2 illustrates that the general trends of eigenvalue shifts with parameter changes do not depend on which of the four parameter regimes is considered, although the details certainly do (such as the quantitative extent to which changing the atmosphere-ocean friction  $R^*$  affects the period). For small perturbations, the change in eigenvalue is linear in the perturbation.

As mentioned in section 2c, the linearization results depend somewhat on the approach used for resetting the atmospheric solver. We have chosen to use the original ZC approach (atmosphere is reset whenever Niño-3 is in the range  $-0.1^\circ$  to  $+0.1^\circ$ ) for consistency with other published literature. Because our initial conditions are chosen with a small amplitude, Niño-3 is always in this range and the resetting happens every

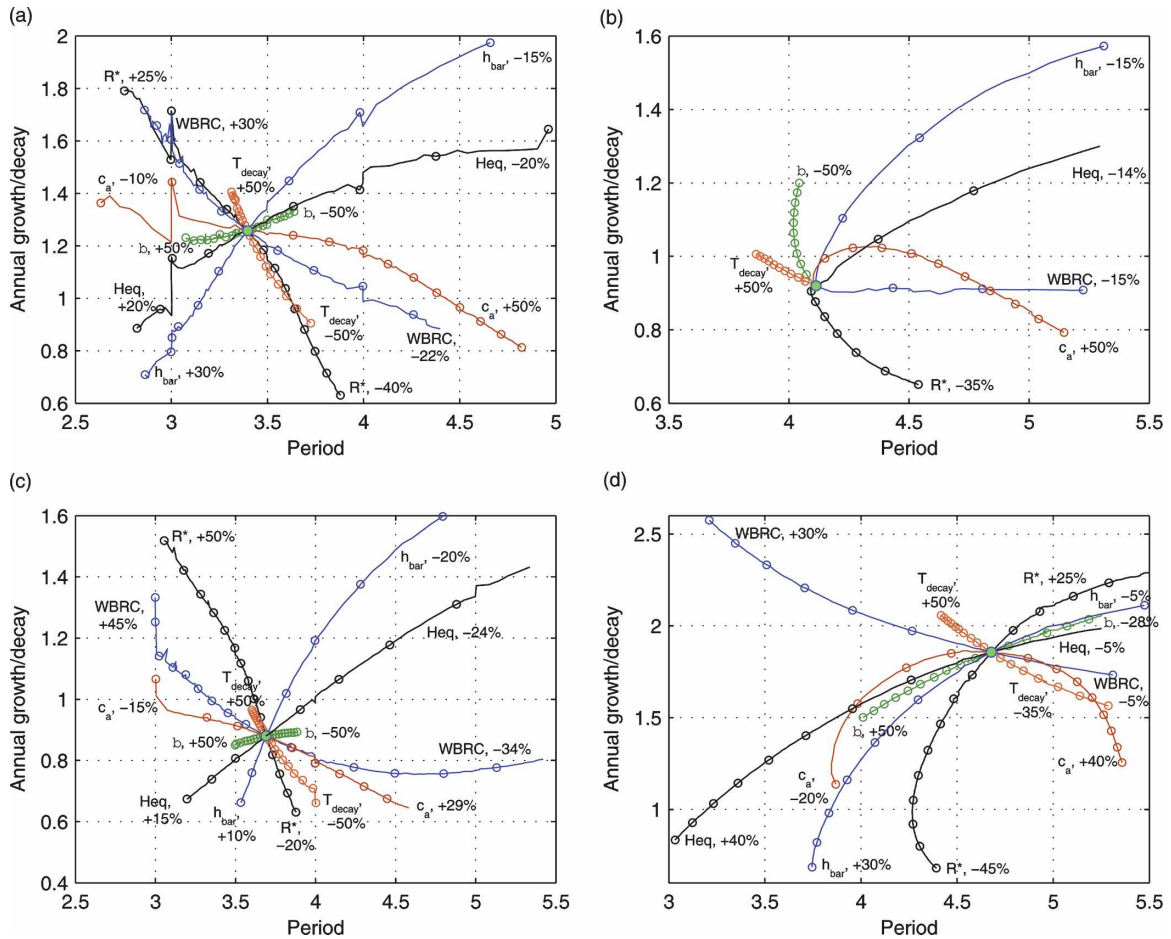


FIG. 2. Root locus plots of the linearized model eigenvalues. The growth rate (eigenvalue magnitude) and period ( $2\pi/\text{eigenvalue}$  phase) are plotted. The colored lines show the eigenvalue variation as a function of different model parameters, with markers placed for every 5% change in the parameter value. For each variable, the % change is also indicated for the final point plotted. (a) Variation around standard parameter values used in the ZC model. (b) Around the annual mean background state. (c) For reduced drag coefficient of  $R^* = 0.75$  resulting in a damped model behavior. (d) Around a permanent July background state.

time step, unlike in the standard ZC model run. Alternatively, if the atmosphere reset is only performed when the Niño-3 index crosses between positive and negative values, then the linearization in the absence of a seasonal cycle is unchanged, but the linearization in the presence of the seasonal cycle exhibits much stronger phase-locking to the seasonal cycle. We considered several additional resetting alternatives and concluded that overall this issue does not seem to affect our main findings. Note that in the figures, some phase-locking is still apparent. This is seen where, as a model parameter is varied, the period remains fixed to a value  $T$  such that  $T/1 \text{ yr} = p/q$ , where  $p$  and  $q$  are integers: for example,  $T = 3, 4$ , or  $3.5 \text{ yr}$  (Tziperman et al. 1995).

For some parameter choices, the ENSO mode is not the dominant eigenvalue and an (approximately) 11-month mode appears (Mantua and Battisti 1995;

Tziperman et al. 1997). This affects the calculated eigenvalues, and the few such points in parameter space where this occurs are not included in our root locus plots. This arises in particular for the annual mean case (Fig. 2b) in which the shift in background climatology that stabilizes the ENSO mode does not similarly stabilize the 11-month mode. As a result, several of the parameter changes explored for the other regimes are not plotted for this regime.

The variation of the eigenvalues as a function of the strength of the seasonal cycle is not plotted in Fig. 2 because it is not as smooth as for the other parameters. As the seasonality amplitude is reduced toward the annual mean or toward permanent July, the eigenvalue changes from the value in regime A to the values in regimes B and D, correspondingly.

The nondimensional damping and period sensitivity

TABLE 2. Nondimensional sensitivity of the eigenvalue period and damping to parameter changes, expressed as % increase in period or growth rate per % increase in parameter value. The strongest sensitivities to period and growth rate are set in boldface.

Parameter	Period sensitivity	Growth rate sensitivity
$R^*$ , $\alpha$	-0.54	<b>1.3</b>
$\beta$	-0.15	-0.1
$\bar{h}$	<b>-0.9</b>	<b>-2.6</b>
$T_{\text{decay}}$	-0.07	0.3
WBRC	<b>-0.9</b>	<b>1.25</b>
$c_a$	<b>1.7</b>	-0.5
$h_{\text{equiv}}$	<b>-1.3</b>	<b>-1.35</b>
SEASC	-0.1	-0.2

(% change in period due to a % change in parameter) are given in Table 2, based on the small change in the parameter part of the results plotted in Fig. 2. We can now make the following general observations regarding parameter sensitivity, based on all of the cases considered (we will later try to physically interpret the computed sensitivities to obtain physical intuition about the dynamics):

- $R^*$ : This parameter primarily affects the damping, with a weak effect on the period that depends on the regime used for the sensitivity study (and therefore is not a robust result).
- $\alpha$ : Its effect is *identical* to changes in  $R^*$ , with a reduction in  $\alpha$  making the system more stable. Note that in the small-amplitude regime in which the atmospheric response to an SST anomaly is linear, the amplitude of the wind stress on the ocean resulting from an SST perturbation  $\Delta T$  is  $(AR^*\alpha)\Delta T$  for some  $A$  representing the effect of the atmospheric dynamics; hence the identical effect of  $\alpha$  and  $R^*$ .
- $\beta$ : The eigenvalue is relatively insensitive to changes in  $\beta$ , with a slightly higher sensitivity for the permanent July regime.
- Mean eastern Pacific thermocline depth: A decrease in the eastern Pacific thermocline depth is destabilizing, with an increase in the period.
- Western boundary reflection coefficient: Decreasing WBRC increases stability and increases the period.
- Atmospheric Rossby radius deformation: Increasing  $c_a$  results in a significant increase in the period.
- Ocean equivalent depth: Increasing  $h_{\text{equiv}}$  results in a significant decrease in the period.
- Ocean momentum damping ( $T_{\text{decay}}$ ): Increasing the decay time is destabilizing, with a decrease in the period.
- Strength of annual cycle: Inconsistent results are observed across parameter regimes. For example, the

case with permanent July conditions is less stable and has a longer period than the seasonal case; the annual mean case is more stable but also has a longer period than the seasonal case.

Model parameters may influence the dynamics through multiple processes; thus the physical interpretation of the impact of changing a given parameter is not always obvious. An instantaneous feedback adjustment can influence the stability or damping of an oscillation, while a parameter perturbation that introduces or changes a delay in the system may be expected to change the period.

Parameters that amplify the ocean-atmosphere coupling, or the response of either of the two, may be expected to affect the stability of the oscillation. This includes  $R^*$  and  $\alpha$ , the thermocline depth, the western boundary reflection coefficient, and the ocean decay time. Reducing the coupling makes the system more stable, as expected from Neelin et al. (1994), Tziperman et al. (1994), Thompson and Battisti (2000), or with the delayed-oscillator model of Suarez and Schopf (1988).

Parameters that affect the delay between the creation of an SST and a wind anomaly and the resulting effect, which eventually reduces the SST anomaly, should affect the oscillation period. This delay includes both ocean wave propagation times (Suarez and Schopf 1988; Battisti 1988) and SST adjustment time (Jin and Neelin 1993b,a; Neelin and Jin 1993). Thus, for example, changing the atmospheric Rossby radius of deformation affects the meridional scale of the wind anomaly and which ocean equatorial Rossby modes get excited, and therefore their travel time (Gill 1982; Kirtman 1997); the linearized period is most sensitive to this parameter. The oceanic equivalent depth affects the period for the same reason. However, the shift in ENSO's period because of changes in the wave propagation delay is significantly larger than the changed wave delay itself (e.g., Kirtman 1997) for reasons discussed in the next section.

The picture, of course, is not simple because most parameters result in changes to both the damping and the period. It is well known from simple models (e.g., Suarez and Schopf 1988) that the ocean-atmosphere coupling also affects the period of ENSO and may even affect the speed of propagation of coupled wave modes (Hirst 1986).

It is clear from the sensitivities that not all of the parameters that affect the ocean-atmosphere coupling affect the period in the same way. An additional factor that influences the model ENSO period can be illustrated by an example. Decreasing the atmosphere-ocean coupling ( $\alpha$  or  $R^*$ ) reduces the amplitude of both

the eastward-propagating oceanic Kelvin wave and the westward-propagating Rossby waves that are excited through the atmospheric response to an SST perturbation. Thus, both the eastern Pacific anomaly caused by the Kelvin component and the canceling effect from the reflected Rossby waves decrease proportionally. The primary effect is to reduce the (Bjerknes) feedback strength and thus increase the damping, without a significant change in any of the time constants. In contrast, decreasing the western boundary reflection coefficient affects both the damping and the period. A reduction in the reflection coefficient reduces only the reflected wave. It therefore takes more time to accumulate a sufficient delayed Rossby wave signal to cancel the eastern Pacific SST perturbation (Cane et al. 1990). Dissipation by a reduced reflection coefficient at the western boundary also reduces the net energy in the system, and thus also increases the damping of the oscillation.

A similar argument appears to be responsible for the period sensitivity of the thermocline depth, described in more detail in the subsequent subsection. A shallower eastern Pacific thermocline leads to higher sea surface temperature sensitivity to thermocline depth perturbations, and therefore greater amplification of anomalies. While this is the main effect of the thermocline depth on the model ENSO, the ENSO period is also increased. In what follows, we illustrate that this is again due to the accumulation delay: the greater amplification of the warm Kelvin wave perturbation in the eastern Pacific requires a greater accumulation of canceling, cold Rossby wave perturbations, which take a longer time to cancel the warm anomaly.

#### b. Period-only and damping-only two-parameter sensitivity experiments

The above sensitivity experiments set the stage for our main objective here, which is to examine factors that affect ENSO's period. For this purpose, we conducted experiments in which two parameters are changed relative to the standard parameters (marked 1 and 2 in Fig. 3), such that the resulting ENSO has a different period but an unchanged damping. Similarly, the experiments marked 3 and 4 in Fig. 3 are characterized by a change to the damping with no related change to the period. The hope is that examining the modification to the eigenvector structure in these experiments relative to the standard case may lead to some insights on physical mechanism(s) that lead to changes in ENSO's period as model parameters are changed.

The eigenvector associated with the dominant ENSO eigenvalue is shown in Fig. 4 for the standard ZC model

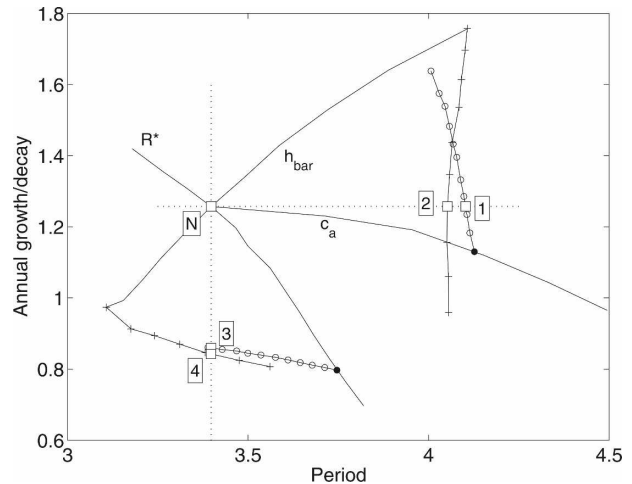


FIG. 3. Eigenvalue growth rate and period illustrating the simultaneous variation of multiple parameters in order to obtain a pure period change without a change in the damping and a pure damping change without a change in the period. Squares indicate the nominal (N) and two experiments that increase the period without changing the damping (1 and 2) and that increase the damping without changing the period (3 and 4). Solid lines indicate varying  $R^*$ ,  $\bar{h}$ , and  $c_a$  with respect to nominal parameters. For experiments 1 and 2, the open-dotted line indicates an increase in  $R^*$ , with  $c_a$  increased by a factor of 1.2, and the crossed line indicates a decrease in  $R^*$  with  $\bar{h}$  decreased by 11.5%. For experiments 3 and 4, the open-dotted line indicates a decrease in  $c_a$ , with  $R^*$  decreased by a factor of 0.7, and the crossed line indicates a decrease in the western boundary reflection coefficient, with  $\bar{h}$  increased by 11.5%.

parameters. The characteristics are broadly similar to the eigenvector information given in Thompson and Battisti (2000; see also Van der Vaart et al. 2000). The imaginary component of both the SST and the atmosphere responses is small compared to the real part. This has to do with the aforementioned choice of the complex amplitude factor used to normalize the eigenvectors such that the real part of the SST vector represents the peak ENSO event. The imaginary part therefore represents the transition between El Niño and La Niña (as in Thompson and Battisti 2000). The small imaginary SST amplitude at this time indicates that the SST response is largely in phase throughout the basin.

The imaginary components of the thermocline depth variation and ocean currents are comparable to their real parts, indicating that these fields have a significant signal during the transition. This is expected from the delayed oscillator–recharge oscillator mechanism, according to which the eastern Pacific equatorial thermocline depth anomaly leads the SST anomaly by a fraction of a cycle, as does the eastward-propagating equatorial Kelvin wave (Suarez and Schopf 1988; Battisti 1988; Jin 1997a; Van der Vaart et al. 2000; Dijkstra 2000).

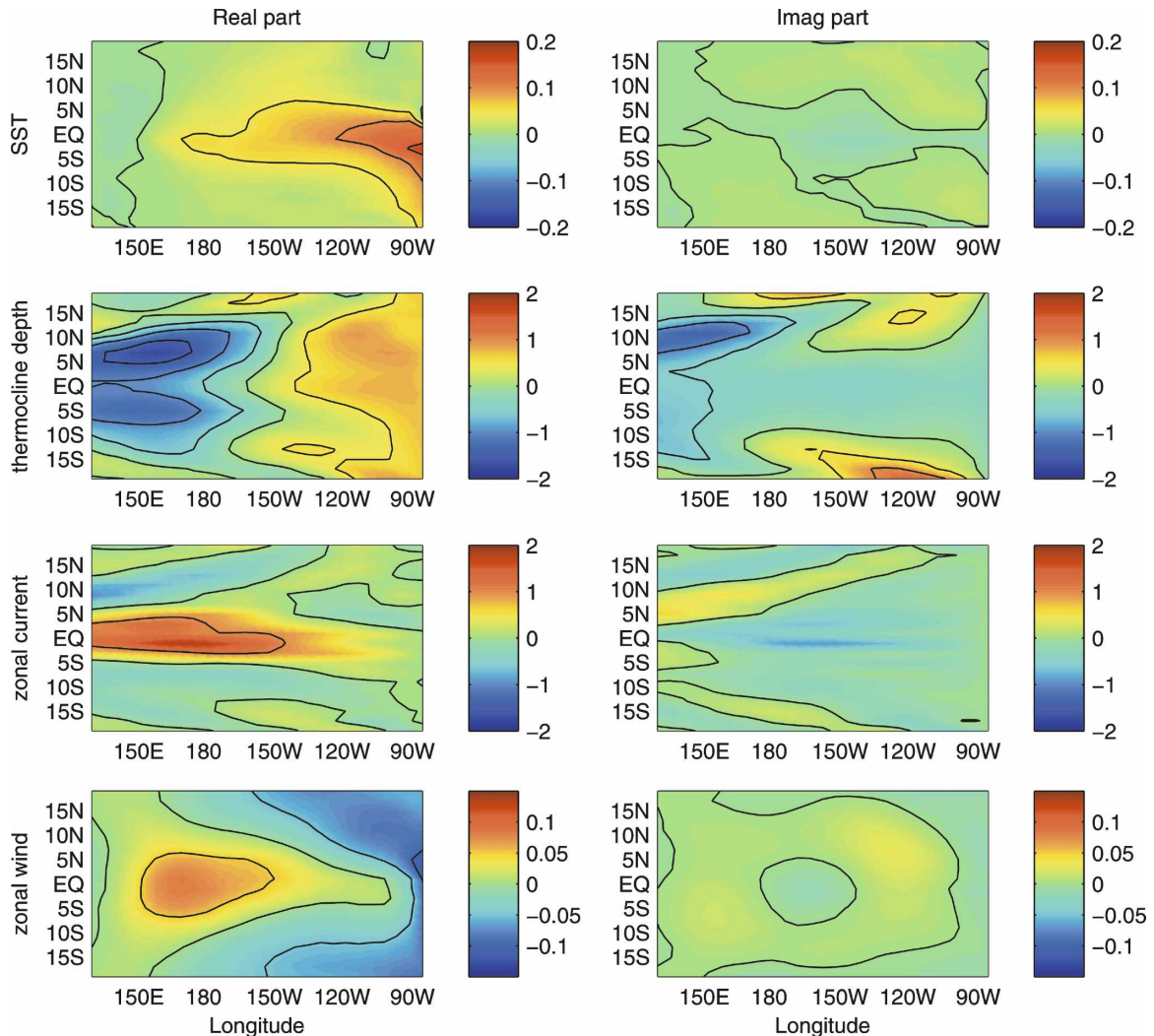


FIG. 4. Eigenvector of the linearized model at standard parameter values for parameter regime A, which are the standard ZC parameter values. The drag coefficient is set to  $R^* = 1$ , and the seasonal cycle is included. The lhs shows the real part of the eigenvector, and the rhs shows the imaginary part. From top to bottom, the pairs of plots are the eigenvector associated with the SST anomaly (contour interval =  $0.05^\circ\text{C}$ ), the thermocline depth anomaly (contour interval =  $0.5\text{ m}$ ), the depth-integrated zonal current anomaly (contour interval =  $1\text{ cm s}^{-1}$ ), and the zonal wind anomaly (contour interval =  $5\text{ cm s}^{-1}$ ).

After projecting the oceanic eigenvector onto the Kelvin, Yanai, and first few Rossby modes (Fig. 5), as in Gill (1983), Battisti (1988), or Tziperman et al. (1998), it is clear that at the Niño-3 peak (real part of eigenvector) there is a positive Kelvin wave signal in the eastern Pacific created by the wind anomaly and a negative Rossby wave signal in the western Pacific, as expected. The first Rossby wave has the highest amplitude, with the amplitudes decreasing with increasing symmetric mode number (the asymmetric Rossby modes are of lower amplitude).

Now consider the eigenvectors corresponding to the experiments that vary two model parameters simultaneously to yield either a pure change in the period with

no change in damping (experiments 1 and 2 in Fig. 3) or a pure change in damping with no change to the period (experiments 3 and 4 in Fig. 3). Our interest here is the processes that determine ENSO's period, and we therefore concentrate on the analysis of experiments 1 and 2. There is no significant difference in the SST component of the eigenvector for any of the parameter-pair changes considered, and therefore there is no easily discernible significant difference in the zonal wind anomalies. The differences in the thermocline depth and zonal current anomaly components of the eigenvectors are more significant and are shown in Figs. 6, 7; in each figure, the two plot pairs correspond to the two experiments in which the period is changed. Each field

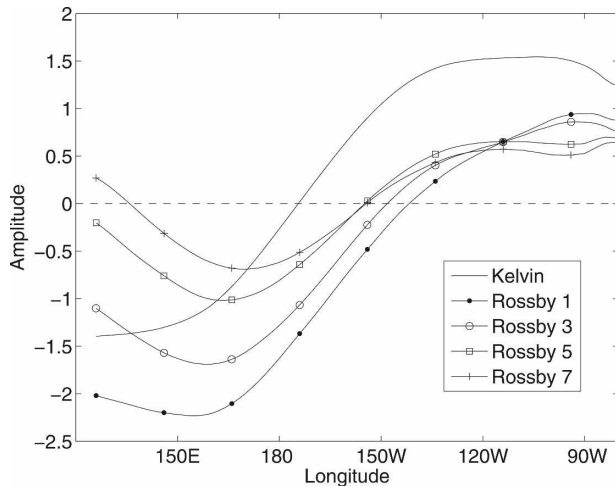


FIG. 5. Projection of the real part of the eigenvector shown in Fig. 4 (corresponding to the linearized solution at the time of Niño-3 maximum) onto ocean Kelvin and Rossby modes for standard parameter values in regime A. Only the symmetric modes have significant response; the first four symmetric Rossby modes are plotted with dots, circles, squares, and crosses.

is normalized by its spatial RMS value before taking the difference.

It should be mentioned that in addition to the plotted change in normalized spatial structure, there is also a change in the relative amplitude between thermocline anomalies, SST anomalies, and current anomalies

within the calculated eigenvectors. Specifically, there is a smaller ocean response for a given SST response in the cases with increased period, but not in the cases with increased damping.

A most interesting result is the robustness of the normalized spatial structure changes of the eigenvector for the experiments in which only the period changes. A comparison of the eigenvector anomaly structure obtained by varying different pairs of parameters (cf. the top pair with the bottom pair in both Figs. 6, 7) shows that the change in the structure of the eigenvector does not depend on which model parameters were changed. The eigenvector change therefore seems to depend only on the degree to which the period changes, rather than on which model parameters were modified to obtain the period change. This suggests that the same physical mechanism is behind the change in period, regardless of which parameters are changed to alter the period.

As we show next, the dominant feature of the eigenvector shift for the cases with increased period is that there is greater lag in the ocean thermocline depth response to the SST and atmospheric winds. The time lag  $t_{\min}(x)$  of the equatorial thermocline minimum at a longitude  $x$  relative to the maximum of the Niño-3 SST index can be directly obtained from the phase of the eigenvector (see appendix B). Figure 8 shows  $t_{\min}(x)$  as a function of longitude  $x$  for several different experi-

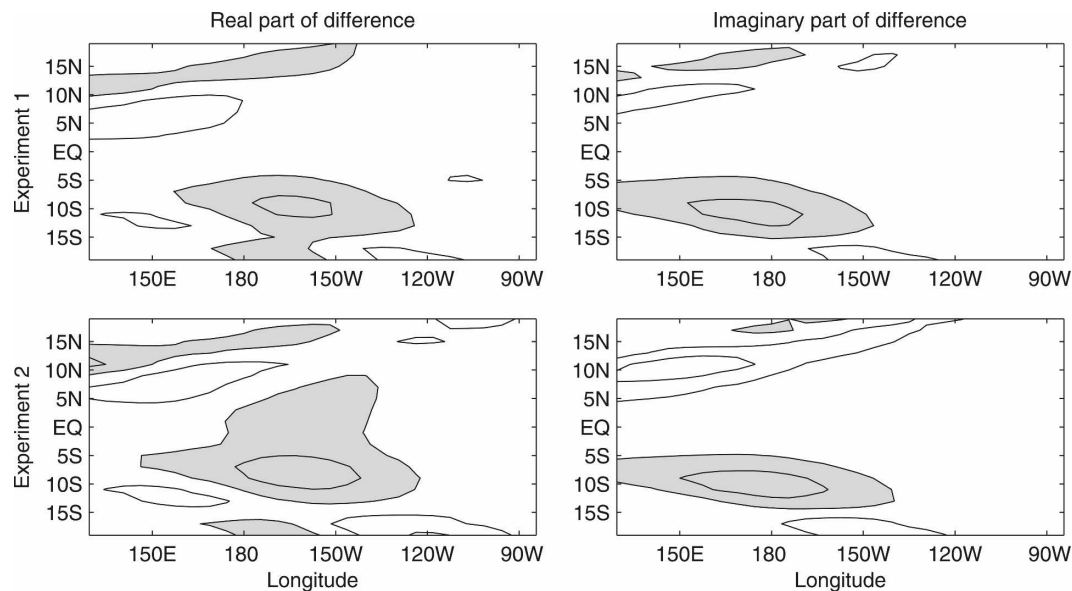


FIG. 6. Comparison of normalized thermocline depth anomaly eigenvector perturbation for two parameter combinations giving a pure shift in period. (top) Experiment 1, involving changes to  $c_a$  and to  $R^*$ ; (bottom) experiment 2, involving changes to the mean thermocline depth and to  $R^*$ . The lhs plots are the difference in the real part of the eigenvector, and the rhs plots show the imaginary part. Contours are  $\pm 0.05$  and  $\pm 0.15$  with regions above  $+0.05$  shaded.

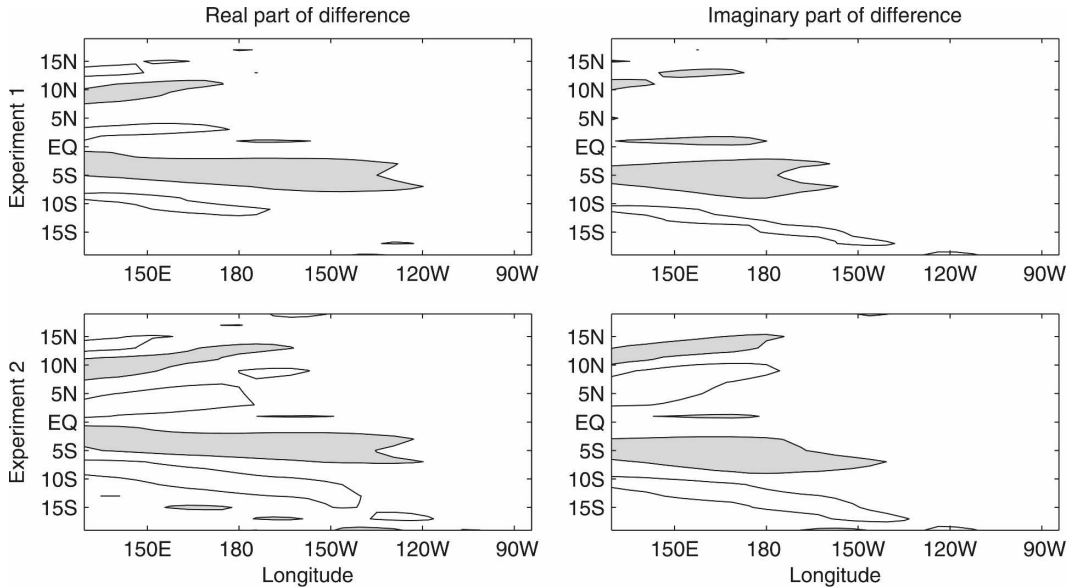


FIG. 7. Comparison of the normalized zonal current anomaly eigenvector perturbation for two parameter combinations giving a pure shift in period. (top) Experiment 1, involving changes to  $c_a$  and to  $R^*$ ; (bottom) experiment 2, involving changes to the mean thermocline depth and to  $R^*$ . The lhs plots are the difference in the real part of the eigenvector, and the rhs plots show the imaginary part. Contours are  $\pm 0.1$  with regions above  $+0.1$  shaded.

ments. Much of our insight comes from this figure and its analysis below. The plotted horizontal lines correspond to the time of the Niño-3 minimum (i.e.,  $T/2$ ).

In the western Pacific, the thermocline anomaly

minimum occurs shortly after the Niño-3 maximum (which is at time = 0 in Fig. 8); the anomaly continues to build up until the atmospheric winds have already begun to slacken. The delay between the SST peak and the minimum thermocline anomaly is determined by the propagation time for the Rossby waves to travel from the midlongitude region where they are created to the western boundary. In the eastern Pacific, however, the thermocline anomaly minimum occurs shortly before the Niño-3 minimum, because it is the decrease in the magnitude of the thermocline anomaly beyond its peak that begins to reverse the SST anomaly. The delay between the eastern thermocline minimum and the Niño-3 minimum is associated with SST dynamics (Jin and Neelin 1993a,b; Neelin and Jin 1993).

It is important to note that the delay between the western thermocline anomaly minimum and the eastern thermocline anomaly minimum is a result of the Kelvin wave propagation time plus the time it takes to accumulate a sufficient deepening signal in the eastern Pacific. This accumulation delay, which is significantly larger than the wave propagation time, is described in detail for a simple model by Cane et al. (1990). There are therefore three factors that together determine delay and hence ENSO's period: the wave propagation delay (see Suarez and Schopf 1988; Battisti 1988), the accumulation delay (Cane et al. 1990), and the SST dynamics delay in the eastern Pacific (Jin and Neelin

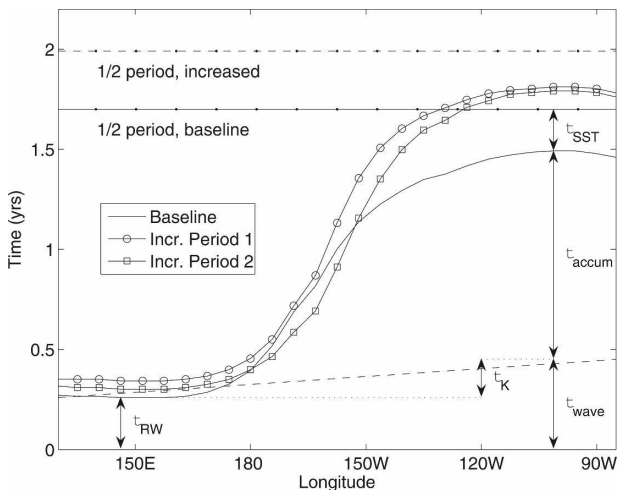


FIG. 8. The time lag between the thermocline minimum peak at a longitude  $x$  relative to the peak of Niño-3, as a function of  $x$ , for several experiments, as reconstructed from the eigenvector analysis. Results are plotted for the baseline parameters of regime A (solid) and for the two cases with an increased period (open circles and squares). The period for each case is shown with horizontal lines. The time delays  $\tau_{\text{wave}} = \tau_{\text{RW}} + \tau_{\text{KW}}$ ,  $\tau_{\text{accum}}$  and  $\tau_{\text{SST}}$  are described in the text.

1993a,b; Neelin and Jin 1993). Changing any combination of these factors will affect the ENSO period.

Figure 8 plots the time lag between the thermocline minimum peak at a longitude  $x$  relative to the peak of Niño-3 for several experiments: the standard case in regime A, which is also the standard ZC parameters (solid line), and the two cases with an increased ENSO period (experiments 1 and 2 in Fig. 3, circles and squares). The three sources of delay noted above are marked with  $\tau_{\text{wave}} = \tau_{\text{RW}} + \tau_{\text{KW}}, \tau_{\text{accum}}$ , and  $\tau_{\text{SST}}$  for the standard parameter case of regime A. The Kelvin wave propagation time  $\tau_{\text{KW}}$  is computed from its wave speed. The important conclusion from this figure is that there is an increase in the length of time it takes for the eastern Pacific equatorial thermocline anomaly to develop in experiments 1 and 2, and this accumulation delay is the most significant contributor to the increased ENSO period for these two sensitivity experiments.

The increased period case from experiment 1 (Fig. 3) involved an increase in the atmospheric wave speed model parameter. This experiment results in a significant additional delay between the Niño-3 peak and the arrival of the peak in the western Pacific thermocline anomaly (i.e.,  $\tau_{\text{RW}}$  is larger for the curve with circles in Fig. 8). This occurs because the change in the atmospheric wave speed changes the atmospheric Rossby radius of deformation, resulting in the excitation of higher Rossby waves in the ocean and correspondingly longer Rossby wave propagation times. This can be verified by projecting the eigenvectors onto the oceanic Kelvin, Yanai, and first few Rossby waves (Fig. 9). The smaller increase in  $\tau_{\text{RW}}$  for experiment 2 appears to be due to an eastward shift in the centroid of the equatorial wind at the Niño-3 peak; the increased travel time for the Rossby waves is consistent with the increase in  $\tau_{\text{RW}}$ .

Figure 9 plots the amplitude of the first few symmetric Rossby modes integrated over the western half of the basin (west of 210°E). The increased period case in which  $\bar{h}$  was changed (experiment 2 in Fig. 3) does not show a significant shift in the relative amplitude of different Rossby components. The increased period case in which the atmospheric wave speed was increased (experiment 1 in Fig. 3) results in roughly 10% higher amplitude for the higher symmetric Rossby modes as compared with the standard case.

The additional delay of the arrival of the reflected “cold” Kelvin wave in the eastern Pacific in experiment 1 has allowed the warm anomaly there to grow stronger. A greater negative feedback signal due to delayed Rossby waves is therefore required to eliminate this stronger signal; hence the longer wave delay can in-

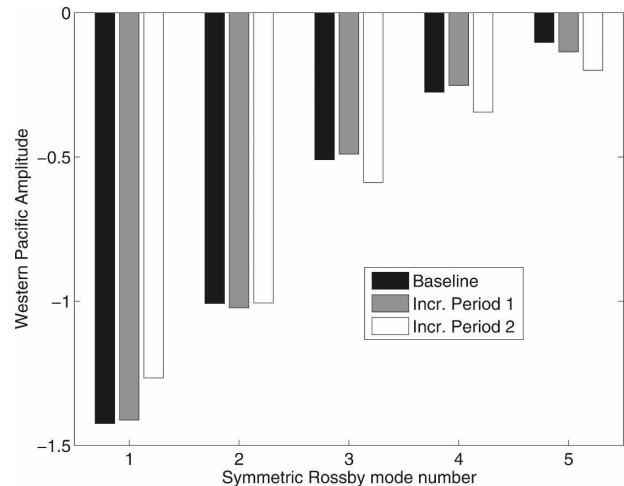


FIG. 9. Amplitude of the projection of the eigenvectors onto symmetric ocean Rossby modes for the eigenvector at the standard parameter values of the ZC model (black) and two at two other parameter choices corresponding to an increased period. Experiment 2 (gray) corresponds to changes to  $\bar{h}$  and  $R^*$ ; experiment 1 (white) corresponds to changes to  $c_a$  and  $R^*$ . The wave amplitudes are integrated over the western Pacific (west of 210°E) and are normalized by the amplitude of the Kelvin wave in the eastern Pacific (east of 210°E).

crease the accumulation delay as well (Cane et al. 1990).

We have examined a simple delayed oscillator model of the type used by Cane et al. (1990), with multiple Rossby modes included, and found that the sensitivity of the period to changes in the amplitude distribution among the Rossby modes is roughly similar to that found here. This confirms that the period indeed changed in experiment 1 because of the changed distribution of energy among the Rossby modes.

The second two-parameter sensitivity experiment with a pure increased period (experiment 2 in Fig. 3) is also plotted in Fig. 8. Here, the period is modified through changes to the mean eastern thermocline depth and to the drag coefficient  $R^*$ , such that the net damping effect vanishes because of the canceling effects of the thermocline depth and the drag coefficient on the coupling strength. The decreased mean depth in the east Pacific increases the growth rate of SST anomalies in the eastern Pacific. This therefore also requires an increase in the time it takes to accumulate a sufficient negative delayed Rossby wave signal to cancel the anomaly. Once again, the dominant change in the period, reflected in the change in the eigenvector, results from changes in the accumulation delay.

The atmosphere–ocean coupling can, in principle, also influence the wave propagation speeds (Hirst 1986); however, we calculated the propagation speeds

of the Kelvin and first few Rossby modes numerically for different coupling strengths and found that these changes are negligible here.

We conclude that the physical mechanism responsible for the period change in experiments 1 and 2 in Fig. 3 is actually different despite the similarity of the eigenvectors. While both experiments predominantly affect the period through increases in the accumulation lag, changes in  $\bar{h}$  and  $R^*$  affect the relative strength of the immediate growth rate and the delayed restoring effect, while changes in  $c_a$  and  $R^*$  affect the wave propagation time. The two experiments are similar in the sense that the accumulation delay is responsible for the changed period in both cases, which the similar eigenvectors reflect.

While we have demonstrated the importance of the accumulation delay using two specific experiments in which only the period varied, the point we are making is more general. The accumulation delay is the longer of the three involved in setting ENSO's period, and therefore it is likely to play a dominant role in any significant period changes. Additional experiments we have carried out varying other parameters in the ZC model confirm this. Furthermore, as we have demonstrated in the above discussion, changes to the SST delay or wave travel time delay will also affect the accumulation delay. Hence, relatively small changes to these other delays may result in a much larger change to the period, via their effects on the accumulation delay.

#### 4. Conclusions

We have explored the effects of many key parameters in the Zebiak–Cane intermediate-complexity model to obtain insight as to what controls ENSO's period. We evaluated the eigenvalues and eigenvectors of the linearized model, and given that the phase of the eigenvalue sets the linear period in a model, we study how this period changes with the different model parameters. Changes in the eigenvector structure that accompany the eigenvalue change are used to understand what determines the period.

Any individual parameter change results in changes in both damping and period, complicating the analysis of parameter perturbations. We therefore introduced sensitivity experiments that involve changing pairs of parameters, chosen to produce changes in the ENSO period with no change in damping, or vice versa.

Our results are best understood by keeping in mind that three different delays together are responsible for ENSO's period: the delay due to the ocean wave propagation times (Suarez and Schopf 1988; Battisti 1988),

the delay required to accumulate a sufficient cold Rossby wave signal in the eastern Pacific to cancel the warm Kelvin wave signal (Cane et al. 1990), and the delay in the SST response to thermocline depth changes in the eastern Pacific (Jin and Neelin 1993a,b; Neelin and Jin 1993). We are able to calculate these separate delays explicitly from the linearized eigenvector analysis.

The key observation from our sensitivity experiments is that all of the parameter choices that affect the period result in an increase in the accumulation delay: the time lag between the peak thermocline anomaly in the western Pacific and the peak thermocline anomaly in the eastern Pacific. This delay is much larger than the Kelvin wave propagation delay and results from the need to accumulate a sufficient Rossby wave thermocline shoaling signal to cancel the eastern Pacific deep thermocline anomaly during an El Niño event (Cane et al. 1990). This is the largest time lag within the modeled ENSO cycle for the standard parameters in the ZC model. The observed shifts in the eigenvector structure indicate that variations in this time lag are responsible for most of the variation in ENSO's period with parameter changes.

The accumulation delay may change because of different physical processes and mechanisms. In our sensitivity experiments these mechanisms depend on which parameters are changed. One example is an increase in the Rossby wave propagation delay, due to changes in the atmospheric Rossby radius. This causes higher and slower equatorial ocean Rossby modes to be excited and therefore allows the eastern Pacific anomaly to grow to larger amplitudes before the Rossby signal starts arriving. The larger warming signal in the east Pacific, in turn, requires a larger accumulation of the cold Rossby wave effect and therefore a longer accumulation delay and a longer period. A second example involves a decrease in the specified mean depth of the eastern Pacific thermocline depth. This results in an increase in the sensitivity of the eastern Pacific SST to thermocline depth perturbations. This greater sensitivity again results in a larger east Pacific warming signal before the Rossby waves start arriving and therefore also requires a longer accumulation delay and a longer period.

We have demonstrated that the accumulation delay may change because of changes in the SST delay and the wave travel time delay. Thus, small changes to these two latter delays may have a larger effect on ENSO's period via the indirect effects of these two delays on the accumulation delay. These conclusions regarding the dominant role of the accumulation delay are more general than the specific sensitivity experiments we have

carried out and provide an interesting insight into ENSO's period.

The insight obtained as well as the methodology used here can, in principle, be applied to more complex general circulation models as well. It would be interesting to compare the accumulation delay in such GCMs and in observations as a tool for improving the simulation of ENSO's period in GCMs.

*Acknowledgments.* We thank Ben Kirtman and an anonymous reviewer for their helpful comments. This work was supported by the James McDonnell Foundation. ET is also supported by NSF Climate Dynamics program, Grant ATM-0351123.

## APPENDIX A

### Algorithm for Identifying the Eigenvalues

The coefficients of the AR model in (7) can be estimated from the model output time series as follows. Here, we consider the more general case in which the output vector  $\mathbf{y}_k$  is not necessarily scalar but of dimension  $M$ , typically small relative to that of the full state vector,  $N_{\text{state}}$ .

Define  $\mathbf{a} = [a_1 \ a_2 \ \dots \ a_N]^T$  and let  $\hat{\mathbf{a}}_k$  be the best estimate of  $\mathbf{a}$ , given the output information up to time step  $k$ . We use a recursive formulation of the AR model fit so that we can test for convergence and use only the minimum simulation time needed to achieve a desired accuracy.

At each time step, define the relevant previous time history as the  $M \times N$  matrix

$$\boldsymbol{\psi}_k = [\mathbf{y}_{k-12} \ \mathbf{y}_{k-24} \ \dots \ \mathbf{y}_{k-12N}], \quad (\text{A1})$$

and update the estimate  $\hat{\mathbf{a}}$  for the AR parameters using the prediction error from Eq. (7) as

$$\hat{\mathbf{a}}_{k+1} = \hat{\mathbf{a}}_k + \mathbf{K}_k(\mathbf{y}_k - \boldsymbol{\psi}_k \hat{\mathbf{a}}_k) \quad (\text{A2})$$

for an  $N \times M$  gain matrix  $\mathbf{K}_k$  to be defined below. The recursive model fit is formulated as a stochastic "system identification" (cf. Kalman filter, e.g., Gelb 1974). Define  $\mathbf{P}$  as the covariance of the error in estimating AR parameters; it is initially large. While the AR parameters are assumed not to change throughout the simulation, each simulation output will not perfectly match (7) even with the perfect estimation  $\hat{\mathbf{a}} = \mathbf{a}$  because of noise resulting from nonlinearities, numerical roundoff error, and the nonzero contributions due to other eigenvector components in the response. Assume this noise to be random with a covariance of

$$\mathbf{R}_k = \boldsymbol{\psi}_k^T \boldsymbol{\psi}_k + \boldsymbol{\epsilon}, \quad (\text{A3})$$

where the noise is assumed to have a part that is proportional to the amplitude (giving rise to the first term on the rhs) and another that is independent (second term). The actual estimation is quite robust to the assumed form. The appropriate Kalman filter gain in (A2) that minimizes the expected estimation error is then

$$\mathbf{K}_k = \mathbf{P} \boldsymbol{\psi}_k (\boldsymbol{\psi}_k^T \mathbf{P} \boldsymbol{\psi}_k + \mathbf{R}_k)^{-1}, \quad (\text{A4})$$

and the updated covariance of the estimation error is

$$\mathbf{P}_{k+1} = (\mathbf{I} - \mathbf{K}_k \boldsymbol{\psi}_k^T) \mathbf{P}_k. \quad (\text{A5})$$

The advantage of the recursive AR formulation over a straightforward least squares formulation is simply that the convergence can be monitored to avoid unnecessary extra simulation.

The overall algorithm, starting from the ZC model, is summarized below. The initial steps are to

- 1) modify the ZC code to include a scale factor  $\gamma$  on the state vector at each time step;
- 2) modify the ZC code to explicitly allow variation in the desired parameters;
- 3) choose  $\gamma$  so that the solution from an arbitrary initial condition is stable and lightly damped; and
- 4) choose an initial condition "close" to the ENSO eigenvector by running the simulation for a moderate number of cycles (until other eigenvectors decay) and scale so that the amplitude of Niño-3 is roughly  $\pm 0.1^\circ\text{C}$  and the simulations are in the linear regime.

Then, for any choice of parameter value, iterate as follows:

- 1) run simulation for a short period of time (we used 50 yr);
- 2) estimate  $\hat{\mathbf{a}}$  and  $\lambda$  as described above;
- 3) exit if converged (sufficiently small change in  $\lambda$ );
- 4) otherwise, rescale the initial condition and use the estimate of  $|\lambda|$  to set  $\gamma$  so that  $\lambda^{12} |\lambda| \approx 0.95$ .

## APPENDIX B

### Calculating the Timing of the West Pacific Thermocline Minimum

Let the eigenvector of the thermocline depth along the equator be  $h_e(x) = h_e^r(x) + ih_e^i(x) = |h_e(x)| e^{i\phi(x)}$  and the imaginary part of the main ENSO eigenvalue be  $\omega_r = 2\pi/T$ . Ignoring the damping at a time  $t$  after the Niño-3 maximum, which corresponds to a phase  $\theta = 2\pi t/T$  of the ENSO cycle with respect to the Niño-3 maximum, the thermocline anomaly at the equator is therefore  $h(x, \theta) = \text{Re}[h_e(x) e^{i\omega_r t}] = \text{Re}[|h_e(x)| e^{i[\phi(x) + \theta]}]$ .

This reaches its minimum at  $\theta + \phi(x) = \pi$ . The time lag of the equatorial thermocline minimum at a longitude  $x$  relative to the maximum of the Niño-3 SST index is thus  $t_{\min}(x) = [\phi(x) - \pi]T$ .

## REFERENCES

- AchutaRao, K., and K. R. Sperber, 2002: Simulation of the El Niño–Southern Oscillation: Results from the coupled model intercomparison project. *Climate Dyn.*, **19**, 191–209.
- , and —, 2006: ENSO simulation in coupled ocean–atmosphere models: Are the current models better? *Climate Dyn.*, **27**, 1–15.
- An, S.-I., A. Timmermann, L. Bejarano, F.-F. Jin, F. Justino, Z. Liu, and A. W. Tudhope, 2004: Modeling evidence for enhanced El Niño–Southern Oscillation amplitude during the Last Glacial Maximum. *Paleoceanography*, **19**, PA4009, doi:10.1029/2004PA001020.
- Battisti, D. S., 1988: Dynamics and thermodynamics of a warming event in a coupled tropical atmosphere–ocean model. *J. Atmos. Sci.*, **45**, 2889–2919.
- Burgers, G., 1999: The El Niño stochastic oscillator. *Climate Dyn.*, **15**, 521–531.
- Cane, M. A., M. Münnich, and S. E. Zebiak, 1990: A study of self-excited oscillations of the tropical ocean–atmosphere system. Part I: Linear analysis. *J. Atmos. Sci.*, **47**, 1562–1577.
- Codron, F., A. Vintzileos, and R. Sadourny, 2001: Influence of mean state changes on the structure of ENSO in a tropical coupled GCM. *J. Climate*, **14**, 730–742.
- Collins, M., and Coauthors, 2005: El Niño– or La Niña–like climate change? *Climate Dyn.*, **24**, 89–104.
- Dijkstra, H. A., 2000: *Nonlinear Physical Oceanography*. Kluwer Academic, 456 pp.
- Doherty, R., and M. Hulme, 2002: The relationship between the SOI and the extended tropical precipitation in simulations of future climate change. *Geophys. Res. Lett.*, **29**, 1475, doi:10.1029/2001GL014601.
- Eccles, F., and E. Tziperman, 2004: Nonlinear effects on ENSO's period. *J. Atmos. Sci.*, **61**, 474–482.
- Fedorov, A. V., and S. G. Philander, 2001: A stability analysis of tropical ocean–atmosphere interactions: Bridging measurements and theory for El Niño. *J. Climate*, **14**, 3086–3101.
- Galanti, E., E. Tziperman, M. Harrison, A. Rosati, R. Giering, and Z. Sirkes, 2002: The equatorial thermocline outcropping—A seasonal control on the tropical Pacific ocean–atmosphere instability strength. *J. Climate*, **15**, 2721–2739.
- Gelb, A., Ed., 1974: *Applied Optimal Estimation*. MIT Press, 388 pp.
- Gill, A. E., 1982: *Atmosphere–Ocean Dynamics*. Academic Press, 662 pp.
- , 1983: An estimation of sea-level and surface-current anomalies during the 1972 El Niño and consequent thermal effects. *J. Phys. Oceanogr.*, **13**, 586–605.
- Hirst, A. C., 1986: Unstable and damped equatorial modes in simple coupled ocean–atmosphere models. *J. Atmos. Sci.*, **43**, 606–630.
- Iooss, G., and D. D. Joseph, 1990: *Elementary Stability and Bifurcation Theory*. 2nd ed. Springer-Verlag, 324 pp.
- Jin, F.-F., 1997a: An equatorial ocean recharge paradigm for ENSO. Part I: Conceptual model. *J. Atmos. Sci.*, **54**, 811–829.
- , 1997b: An equatorial ocean recharge paradigm for ENSO. Part II: A stripped-down coupled model. *J. Atmos. Sci.*, **54**, 830–847.
- , and J. D. Neelin, 1993a: Models of interannual tropical ocean–atmosphere interaction—A unified view. Part I: Numerical results. *J. Atmos. Sci.*, **50**, 3477–3503.
- , and —, 1993b: Models of interannual tropical ocean–atmosphere interaction—A unified view. Part III: Analytical results in fully coupled cases. *J. Atmos. Sci.*, **50**, 3523–3540.
- , —, and M. Ghil, 1994: ENSO on the devil's staircase. *Science*, **264**, 70–72.
- , —, and —, 1996: El Niño/Southern Oscillation and the annual cycle: Subharmonic frequency-locking and aperiodicity. *Physica D*, **98**, 442–465.
- Kang, I.-S., and S.-I. An, 1998: Kelvin and Rossby wave contributions to the SST oscillation of ENSO. *J. Climate*, **11**, 2461–2469.
- Kevrekidis, I. G., C. W. Gear, J. M. Hyman, P. G. Kevrekidis, O. Runborg, and C. Theodoropoulos, 2003: Equation-free coarse-grained multiscale computation: Enabling microscopic simulators to perform system-level tasks. *Comm. Math. Sciences*, **1**, 715.
- , —, and G. Hummer, 2004: Equation free: The computer-aided analysis of complex multiscale systems. *AIChE J.*, **50**, 1346–1355.
- Kirtman, B. P., 1997: Oceanic Rossby wave dynamics and the ENSO period in a coupled model. *J. Climate*, **10**, 1690–1704.
- , and P. S. Schopf, 1998: Decadal variability in ENSO predictability and prediction. *J. Climate*, **11**, 2804–2822.
- Kleeman, R., and A. M. Moore, 1997: A theory for the limitation of ENSO predictability due to stochastic atmospheric transients. *J. Atmos. Sci.*, **54**, 753–767.
- Mantua, J. N., and D. S. Battisti, 1995: Aperiodic variability in the Zebiak–Cane coupled ocean–atmosphere model: Air–sea interactions in the western equatorial Pacific. *J. Climate*, **8**, 2897–2927.
- Münnich, M., M. A. Cane, and S. E. Zebiak, 1991: A study of self-excited oscillations of the tropical ocean–atmosphere system. Part II: Nonlinear cases. *J. Atmos. Sci.*, **48**, 1238–1248.
- Neelin, J. D., and F.-F. Jin, 1993: Models of interannual tropical ocean–atmosphere interaction—A unified view. Part II: Analytical results in the weak-coupling limit. *J. Atmos. Sci.*, **50**, 3504–3522.
- , M. Latif, and F.-F. Jin, 1994: Dynamics of coupled ocean–atmosphere models: The tropical problem. *Annu. Rev. Fluid Mech.*, **26**, 617–659.
- , F.-F. Jin, and H.-H. Syu, 2000: Variations in ENSO phase locking. *J. Climate*, **13**, 2570–2590.
- Penland, C., and P. D. Sardeshmukh, 1995: The optimal growth of tropical sea surface temperature anomalies. *J. Climate*, **8**, 1999–2024.
- Philander, S. G., and A. Fedorov, 2003: Is El Niño sporadic or cyclic? *Annu. Rev. Earth Planet. Sci.*, **31**, 579–594.
- Samelson, R. M., and E. Tziperman, 2001: Predictability of the chaotic ENSO: The growth-phase predictability barrier. *J. Atmos. Sci.*, **58**, 3613–3625.
- Suarez, M. J., and P. S. Schopf, 1988: A delayed action oscillator for ENSO. *J. Atmos. Sci.*, **45**, 3283–3287.
- Syu, H. H., and J. D. Neelin, 2000: ENSO in a hybrid coupled model. Part I: Sensitivity to physical parameterizations. *Climate Dyn.*, **16**, 19–34.
- Thompson, C. J., and D. S. Battisti, 2000: A linear stochastic dynamical model of ENSO. Part I: Model development. *J. Climate*, **13**, 2818–2832.

- , and —, 2001: A linear stochastic dynamical model of ENSO. Part II: Analysis. *J. Climate*, **14**, 445–466.
- Timmermann, A., J. Oberhuber, A. Bacher, M. Esch, M. Latif, and E. Roeckner, 1999: Increased El Niño frequency in a climate model forced by future greenhouse warming. *Nature*, **398**, 694–697.
- , S. I. An, U. Krebs, and H. Goosse, 2005: ENSO suppression due to weakening of the North Atlantic thermohaline circulation. *J. Climate*, **18**, 3122–3139.
- Tziperman, E., L. Stone, M. A. Cane, and H. Jarosh, 1994: El Niño chaos: Overlapping of resonances between the seasonal cycle and the Pacific ocean–atmosphere oscillator. *Science*, **264**, 72–74.
- , M. A. Cane, and S. E. Zebiak, 1995: Irregularity and locking to the seasonal cycle in an ENSO prediction model as explained by the quasi-periodicity route to chaos. *J. Atmos. Sci.*, **52**, 293–306.
- , H. Scher, S. E. Zebiak, and M. A. Cane, 1997: Controlling spatiotemporal chaos in a realistic El Niño prediction model. *Phys. Rev. Lett.*, **79**, 1034–1037.
- , M. A. Cane, S. E. Zebiak, Y. Xue, and B. Blumenthal, 1998: Locking of El Niño’s peak time to the end of the calendar year in the delayed oscillator picture of ENSO. *J. Climate*, **11**, 2191–2199.
- Van der Vaart, P. C. F., H. A. Dijkstra, and F. F. Jin, 2000: The Pacific cold tongue and the ENSO mode: A unified theory within the Zebiak–Cane model. *J. Atmos. Sci.*, **57**, 967–988.
- Wang, B., A. Barcilon, and Z. Fang, 1999: Stochastic dynamics of El Niño–Southern Oscillation. *J. Atmos. Sci.*, **56**, 5–23.
- Zebiak, S. E., and M. A. Cane, 1987: A model El Niño–Southern Oscillation. *Mon. Wea. Rev.*, **115**, 2262–2278.